Electrically and thermally tunable multifunctional terahertz metasurface array

Yue Wang,[1,2] Dajian Cui,[3] Yu Wang,[1,2] Guohui Yang,[4] and Chunhui Wang[1,2,*]

[1]*National Key Laboratory of Tunable Laser Technology, Harbin Institute of Technology, Harbin, Heilongjiang, 150001, China*

[2]*Glint Institute of Artificial Intelligence and Robotics, Shenzhen, Guangdong, 518063, China*

[3]*The 44th Research Institute of China Electronics Technology Group Corporation, Chongqing, 400060, China*

[4]*The School of Electronic and Information Engineering, Harbin Institute of Technology, Harbin, Heilongjiang, 150001, China*

(Received 3 January 2022; accepted 8 March 2022; published 23 March 2022)

In this paper we propose a kind of all-solid-state and a hybrid electrically and thermally tunable multifunctional metasurface array based on the graphene pattern and vanadium dioxide configuration, which can realize the functions of band-stop filtering, beam steering, and beam splitting. When VO_2 is in the dielectric state, this metasurface can be used as an angle-insensitive filter that can realize the function of the dual-frequency adjustable band-stop filtering by changing the Fermi level of graphene in the range of 4.11–6.51 THz. When VO_2 is in the metal state, this metasurface can be used as a terahertz phased array device. By changing the Fermi level of graphene and the phase distribution, it is proved that this metasurface can achieve a specific deflection angle, a continuous scanning range of 0–68.37°, or beam splitting at angles of ±25.56° and ±59.29°. Our work shows great potential in the field of multifunctional integrated chips.

DOI: 10.1103/PhysRevA.105.033520

I. INTRODUCTION

In recent decades, terahertz (THz) technology has attracted significant attention because of its potential applications in spectroscopy [1,2], imaging [3,4], biosensors [5,6], and high-speed wireless communication [7]. This progress has also prompted the development of low-cost, compact, and low-complexity THz photonic devices such as filters [8–10] and THz phased arrays (TPAs) [11–13]. The filter is a device that allows perfect transmission in a narrow frequency interval and prevents any radiation outside the passband, or allows perfect transmission in a wide frequency interval and zero transmission in a narrow frequency interval. The TPA is used to control the deflection angle of incident electromagnetic waves, which is realized by different predesigned phase gradients. However, the development of THz devices with high-speed and low-cost performance is still elusive compared with microwave technology.

To meet this requirement, metasurfaces, especially active metasurfaces, have been proposed to develop THz devices [14–17]. Metasurfaces were first investigated as passive photonic elements that can control the amplitude, phase, and polarization of transmitted or reflected electromagnetic waves [18,19]. Then they gradually evolved into active metasurfaces by exploring liquid-crystal materials [20,21], semiconductor materials [22], phase change materials [23,24], and graphene materials [25–27] because the function of passive metasurfaces is fixed once manufacturing is completed.

Graphene and VO_2 are two representative materials to realize electric and temperature control in all adjustable metasurface architectures. Graphene, a single-layer carbon atom arranged in a two-dimensional hexagonal lattice material, has attracted much attention due to its fast carrier mobility, high optical transparency, and tunability properties in chemistry, energy, materials, and physics [28]. Yang *et al.* [29] proposed a micromachined tunable THz filter by combining periodic metallic rings with several gaps and tunable graphene stripes. Using numerical simulations and experiments, they showed that the resonance frequency of the structure can be altered from 0.2 THz to 0.12 THz by simply tuning the conductivity of graphene. Orazbayev *et al.* [30] demonstrated tunable midinfrared beam steering devices based on multilayer graphene-dielectric metamaterials. The operating principle is that the spatial distribution of the phase of the transmitted beam can be arbitrarily tailored by changing the chemical potential of each graphene layer. As a phase change material, VO_2 can change from insulator state to metal state at a critical temperature of around 340 K [31]. During this process, the conductivity of VO_2 increases by several orders of magnitude because the lattice changes from a monoclinic to a tetragonal structure with the increase of temperature. Similarly, VO_2 can also be used to design adjustable filters and beam controllers. Huang *et al.* [32] and Kaplan *et al.* [33] proposed a THz metamaterial bandpass filter with an actively controlled bandwidth and a tunable optical phased array antenna for beam steering applications by utilizing the properties of VO_2.

In fact, many THz devices based on graphene and VO_2 metasurfaces have been proposed [34–39]. Still, most of them can only realize a single adjustable function, which affects the further integration of THz devices. In this work we propose a multifunctional THz device composed of an electrically tunable patterned graphene plasmonic metasurface and a thermally tunable VO_2 back reflector. An active THz filter and a TPA are integrated into a single structure. They can be

*wangch_hit@163.com

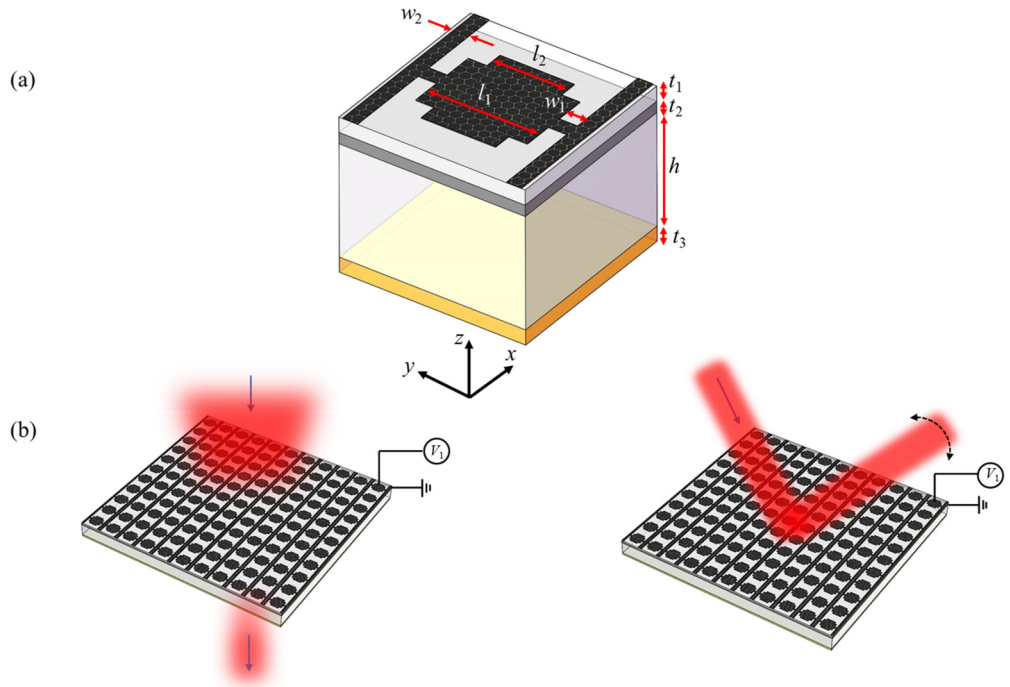

FIG. 1. Structure of the proposed metasurface. (a) Unit cell of the metasurface. (b) Active metasurface array composed of a series of electrically tunable supercell periods.

switched freely and regulated independently by applying different temperatures to VO_2 at the bottom layer and different bias voltages to graphene at the top layer. Detailed numerical investigations reveal that a careful selection of the operating ranges for bias voltages of graphene allows us to assign the voltages to adjust the center wavelength of the filter or the beam steering of the TPA, whereas the temperature of VO_2 is used to convert the two functional devices. Utilizing temperature and voltage as two separate control modes, we achieve a dual-band band-stop filter with an adjustable central frequency of 4.11–6.51 THz and a TPA with specific or continuous sweep beam deflection between 0 and 68.37° and beam splitting at 25.56° and 59.29°. This metasurface that can integrate functions of band-stop filtering, beam deflection, and beam splitting simultaneously may open up a way for the integration of THz multifunctional devices.

II. STRUCTURE DESIGN AND SIMULATION METHODS

The tunable multifunctional THz metasurface presented here comprises a patterned graphene antenna array, SiO_2 spacers, electrode layer, SiO_2 dielectric layer, and VO_2 film substrate from top to bottom. As illustrated in Fig. 1, the central part of the graphene pattern is designed as a cross and the second part is a continuous graphene narrowband to connect the applied bias voltage. The period p of the unit cell is 5 μm in both the x and y directions, which ensures that the absorption resonance will be located at the THz band.

The structural parameters of the graphene pattern layer are characterized by $l_1 = 3.00$ μm, $l_2 = 2.00$ μm, $w_1 = 0.60$ μm, and $w_2 = 0.35$ μm. The surface conductivity of the single-layer graphene can be obtained by the Kubo formula, including the intraband σ_{intra} and interband σ_{inter} parts [40]

$$\sigma(\omega, E_F, \tau, T) = \sigma_{\text{intra}}(\omega, E_F, \tau, T) + \sigma_{\text{inter}}(\omega, E_F, \tau, T) = \frac{-ie^2}{\pi\hbar(\omega + i2\tau)} \int_0^\infty \xi \left[\frac{\partial f_d(\xi)}{\partial \xi} - \frac{\partial f_d(-\xi)}{\partial \xi} \right] d\xi + \frac{ie^2(\omega + i2\tau)}{\pi\hbar^2} \int_0^\infty \xi \frac{f_d(-\xi) - f_d(\xi)}{(\omega + i2\tau)^2 - 4\left(\frac{\xi}{\hbar}\right)^2} d\xi, \quad (1)$$

where $f_d(\xi)$ is the Fermi-Dirac distribution, which can be expressed as

$$f_d(\xi) = \frac{1}{\exp[(\xi - E_F)/k_B T] + 1}. \quad (2)$$

In these two formulas, ω represents the radian frequency, e represents the electron charge, $\hbar$ represents the reduced Planck constant, $T = 300$ K is the temperature, $\tau = 1$ is the relaxation time, k_B represents the Boltzmann constant, and $E_F = \mu_c$ is the Fermi energy which can be adjusted by applying an external bias voltage. The SiO_2 in the upper layer is used as the insulating medium to isolate the graphene layer and the electrode layer and its thickness and refractive index are $t_1 = 0.10$ μm and $n = 1.97$, respectively [41]. We select two schemes, which are polysilicon [42] and metal mesh structure [43], as the electrode layer of the device,

and the results of the two schemes are consistent through simulation. Here we take the polysilicon as the electrode layer for follow-up simulation research in this paper but will leave determination of the final electrode scheme according to the experimental results for future work. The thickness of polysilicon is set to $t_2 = 0.05\ \mu$m during the simulation. The SiO_2 in the lower layer is used as the dielectric layer of the metasurface and its thickness is $h = 4.50\ \mu$m. Finally, the thickness of VO_2 film is $t_3 = 0.30\ \mu$m. The Drude model is used to describe the properties of VO_2 in the THz range [44], as expressed by

$$\varepsilon(\omega) = \varepsilon_\infty - \frac{\omega_p^2(\sigma)}{\omega^2 + i\gamma\omega}, \tag{3}$$

where $\varepsilon_\infty = 12$ is the permittivity at high frequency and $\gamma = 5.75 \times 10^{13}$ rad/s is the collision frequency. The plasma frequency ω_p can be approximately described as

$$\omega_p^2(\sigma) = \frac{\sigma}{\sigma_0}\omega_p^2(\sigma_0),$$
$$\sigma_0 = 3 \times 10^5\ \text{S/m},$$
$$\omega_p(\sigma_0) = 1.4 \times 10^{15}\ \text{rad/s}. \tag{4}$$

In this paper VO_2 is modeled as a material with a permittivity of 9 in the insulator phase when the temperature is lower than 340 K and with a conductivity of 3×10^5 S/m in the metal phase when the temperature is higher than 340 K, which can be achieved in the experiments. In addition, the incident light is set to perpendicular to the metasurface with the E_x polarization direction in all the simulation processes in this paper due to the polarization sensitivity of the metasurface, which is caused by the destruction of the antenna structure. The numerical simulations of the proposed metasurface are first performed using CST MICROWAVE STUDIO using the finite-element method in a metasurface element design. The unit cell conditions are set in the x and y directions, while the open (add space) is set in the z direction. The VO_2 film can be coated by magnetron sputtering deposition in subsequent experiments. The graphene film prepared by chemical vapor deposition (CVD) will be transferred to the surface of SiO_2 by the wet transfer technology, and gas plasma etching technology will be used to prepare graphene structures. To provide the designed bias voltage for the graphene structure layer, we connect the polysilicon layer to the zero voltage and connect the graphene structure of each column as a supercell to the equipotential voltage. In addition, a spacing of 0.10 μm is set between each column of graphene to prevent voltage crosstalk.

III. SIMULATION RESULTS AND DISCUSSION

A. Active THz filter function

This device can realize the function of a tunable dual-band band-stop filter when VO_2 is in the insulator state with a temperature lower than 340 K. Figure 2 shows the simulated filter frequency response for graphene Fermi levels of 0.30, 0.35, and 0.40 eV. It can be observed that the device shows band-stop characteristics at frequencies 4.87 and 5.45 THz and its transmittance is 12.1% and 6.2%, respectively. In comparison, it offers a high bandpass with transmittance more significant than 80% at other frequencies between 3.0 and 7.5

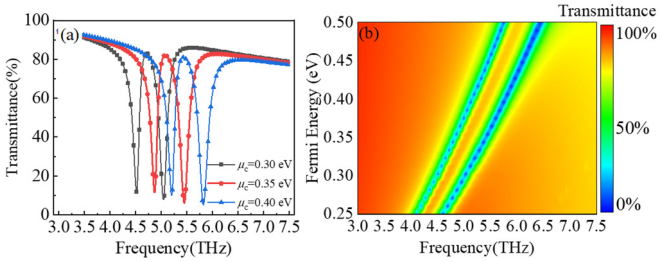

FIG. 2. (a) Simulated transmittance versus frequency when the Fermi levels of graphene are 0.30, 0.35, and 0.40 eV. (b) Contour plot of transmittance with the variation of frequency and Fermi energy level.

THz when the graphene Fermi level is 0.35 eV. In addition, the two band-stop frequencies can be blueshifted and redshifted, respectively, when the Fermi level of graphene increases and decreases. As the black curve with squares and blue curve with triangles in Fig. 2(a) show, the device's center frequencies are shifted to 4.52 and 5.04 THz and 5.20 and 5.82 THz when the Fermi levels of graphene are changed to 0.30 and 0.40 eV, respectively. It should be noted that these simulation results are obtained under the condition of taking the same Fermi level for graphene on the whole metasurface.

After the simulation of all the transmittance curves between 0.25 and 0.50 eV in steps of 0.01 eV, we draw the contour plot of the transmittance of the device with the frequency and the Fermi level of graphene shown in Fig. 2(b). This device can achieve fixed or continuously changing dual-frequency band-stop characteristics in the range of 4.11–6.51 THz by adjusting the Fermi level of graphene. With the assumption that the incident electromagnetic wave is vertical, we obtain the above results by simulation, but the incident angle of the target electromagnetic wave cannot be guaranteed to be 0 in practical application. Therefore, we simulate the filtering characteristics under different incident angles. Figure 3 shows that the transmittance curve of the device will only change slightly when the incident electromagnetic wave angle increases to 30° in both the x and y directions. In addition, compared with the traditional angle-insensitive metasurface filter [45,46], the adjustable filter proposed in this paper can not only have the characteristics of angle insensitivity in both the x and y directions but also maintain

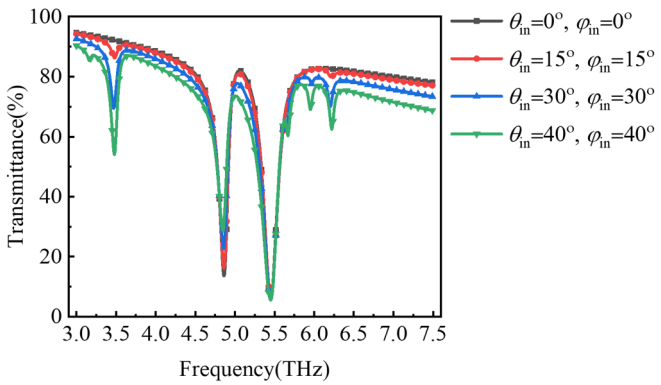

FIG. 3. Simulated transmittance curves for different incident angles.

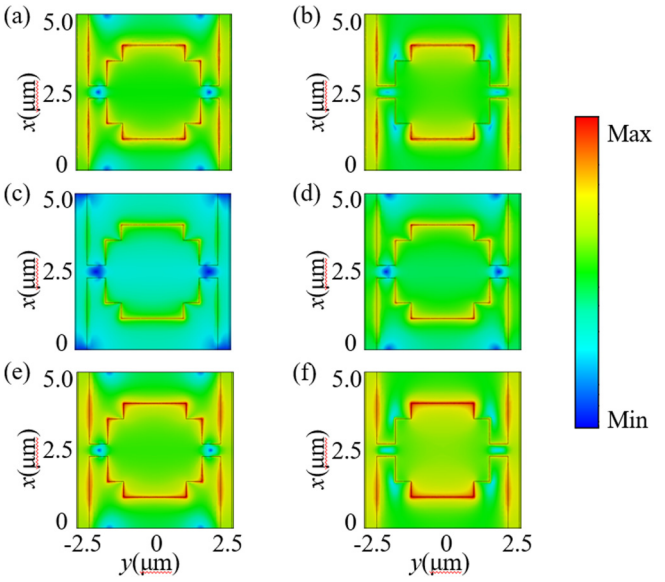

FIG. 4. Electric-field distribution at (a) $f = 4.52$ THz and $\mu_c = 0.30$ eV, (b) $f = 5.04$ THz and $\mu_c = 0.30$ eV, (c) $f = 4.52$ THz and $\mu_c = 0.40$ eV, (d) $f = 5.04$ THz and $\mu_c = 0.40$ eV, (e) $f = 5.20$ THz and $\mu_c = 0.40$ eV, and (f) $f = 5.82$ THz and $\mu_c = 0.40$ eV.

uniform band-stop adjustability after changing the angle of the incident electromagnetic wave. To better understand the resonance phenomenon and the band-stop frequency control characteristics of the metasurface, the surface electric-field distributions under different Fermi levels of graphene are simulated, respectively. When the Fermi level of graphene is 0.3 eV, the phenomena of high-intensity electric-field aggregation and electric dipole resonance can be clearly observed at $f = 4.52$ and 5.04 THz, as shown in Figs. 4(a) and 4(b), respectively. This means that electromagnetic resonance occurs at these frequencies and supports the premise of band-stop characteristics and subsequent phase mutation characteristics. The difference between the electromagnetic resonance of the two frequencies is at $f = 4.52$ THz. The charge focusing position appears at the edge between the graphene cross and the graphene electrode band. In contrast, at frequency $f = 5.04$ THz, the charge accumulation position occurs at the upper and lower ends of the graphene cross. The simultaneous resonance of these two positions endows the metasurface with dual-frequency band-stop characteristics.

As shown in Figs. 4(c) and 4(d), when we increase the Fermi level of graphene to 0.4 eV, no apparent electric-field aggregation is observed at $f = 4.52$ THz and only slight electric-field aggregation is observed at $f = 5.04$ THz. This phenomenon shows no apparent resonance phenomenon and band-stop characteristics at these two frequencies. However, if the electric-field distribution frequency is changed to $f = 5.20$ and 5.82 THz, it is found that the electric-field aggregation phenomenon will reappear at the same position as before, as shown in Figs. 4(e) and 4(f). The reemergence of this resonance phenomenon proves that when the Fermi level of graphene changes, the center frequency of electromagnetic resonance caused by electric-field focusing will shift instead of the resonance completely disappearing. This frequency shift of the electric-field aggregation phenomenon is also why the center frequency of the band stop and subsequent phase mutation is shifted.

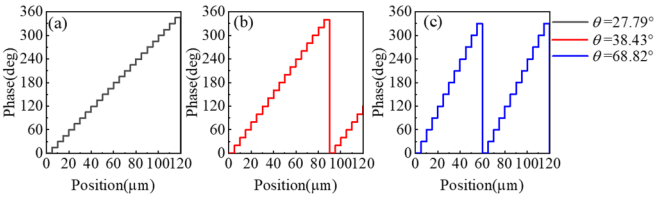

FIG. 5. Theoretical results of the phase corresponding to deflection angles of (a) 27.79°, (b) 38.43°, and (c) 68.82° according to a period of 360°.

B. TPA for beam steering

This device can realize the function of the TPA when VO_2 is in the metal phase with a temperature higher than 340 K. To realize the beam deflection function of the TPA by using the metasurface, we first calculate the phase gradient of the metasurface element according to the target deflection angle. The relationship between phase gradient and deflection angle can be expressed as [47]

$$\varphi(x) = k_0 x \sin\theta = \frac{2\pi}{u} f_0 x \sin\theta, \tag{5}$$

where x is the relative position, k_0 is the wave number, f_0 is the frequency of the incident electromagnetic wave, u is the wave velocity, θ represents the deflection angle of the target, and φ represents the phase of the desired position. To show the relationship between the metasurface unit phase and the deflection angle conveniently, 27.82°, 38.48°, and 68.96° are selected as the target deflection angles when $f = 5.35$ THz. Then the calculated phase curve is converted into a 360° period to facilitate unification, and the value is stepped with a width of $p = 5$ μm, as shown in Fig. 5. To achieve the designed phase gradient to realize the beam deflection function, the phase control range of the metasurface needs to reach almost 360°. Therefore, we simulate the reflectivity curves and reflection phase curves under different graphene Fermi levels when VO_2 is in the metal state at the second step; the results are shown in Fig. 6. In this simulation process, the material properties of VO_2 on the metasurface are only converted while any other structural parameters are not changed. When the Fermi level of graphene on the whole metasurface is set to 0.35 eV, there are two resonance frequency points of 4.78 and 5.40 THz, that is, two

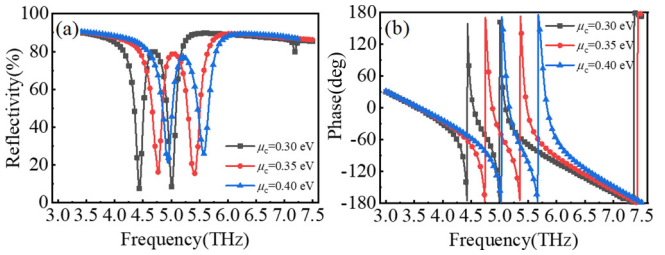

FIG. 6. Metasurface (a) reflectivity curves and (b) reflection phase curves when the Fermi energy levels of graphene are 0.3, 0.35, and 0.4 eV.

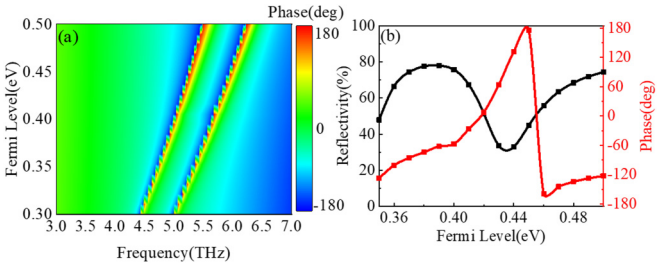

FIG. 7. (a) Contour plot of the reflection phase with the frequency and the Fermi level of graphene. (b) Reflectivity curves and reflection phase curves at different graphene Fermi levels when $f = 5.35$ THz.

phase mutation frequency points. This phenomenon makes it possible to obtain a phase change of nearly 360° between the two resonant frequency points, corresponding to different frequencies. When we change the Fermi level of graphene to 0.30 and 0.40 eV, the reflectivity curve and phase curve will be redshifted and blueshifted and the two resonance frequency points will be shifted to 4.44 and 5.01 THz and 5.08 and 5.74 THz, respectively. This characteristic of the adjustable center frequency is the basis of realization of a solid-state adjustable TPA. In addition, the principle of this resonance phenomenon and resonance frequency offset is similar to the filter, so it will not be repeated here. Subsequently, we simulate the phase curve of the graphene Fermi level from 0.3 to 0.5 eV and draw the results as a contour plot of the reflection phase with the frequency and the Fermi level of graphene, as shown in Fig. 7(a). The designed metasurface can achieve 360° phase regulation by changing the Fermi level of graphene in the frequency range of 4.4–6.5 THz. The difference in beam deflection function at different frequencies only shows the corresponding relationship between the Fermi level and phase. Here we take $f = 5.35$ THz as an example to design the TPA. The reflectivity curves and reflection phase curves at different graphene Fermi levels are extracted, as shown in Fig. 7(b), when the target frequency is set to 5.35 THz. The phase curve gradually increases from −120° to 180°, then jumps to −172°, and then gradually increases to −120° when the Fermi level of graphene gradually increases from 0.35 THz to 0.50 THz. This shows that the metasurface can realize 352° phase regulation. Moreover, the maximum reflectivity change is only 44.9% in this phase change range, which is beneficial to reduce the side lobe of the TPA. So far, we can use the designed metasurface to realize the beam deflection function of the TPA. First, we set each column of cells on the metasurface as a supercell and apply the same bias voltage to each supercell, making the supercell obtain the same Fermi level and phase, as shown in the right image in Fig. 1(b). Second, the phase required for each supercell is determined according to the relationship between the phase gradient and the beam deflection angle shown in Fig. 5. For example, for a beam deflection angle of 68.37°, the supercell needs to gradually increase from 0 to 360° with a phase gradient of 30° and continue to extend outward as a period. Then the graphene Fermi level corresponding to the required phase of each supercell is found according to the red curve with squares in Fig. 7(b). Finally, we simulate all the designed metasurface arrays using FDTD software. During the simulation, the device is excited by a linearly-E_x-polarized plane wave that impinges at normal incidence concerning the surface in the z direction. We set the boundary conditions in the x and y directions as the periodic boundary, set the boundary conditions in the z direction as a perfectly matched layer boundary, and set the number of layers to 64 to absorb all additional electromagnetic wave energy. In addition, we set the structure to periodic and the illumination to a Gaussian spot in the far-field setting.

The final simulation curves and far-field results are shown in Fig. 8. The simulation results show that the designed TPA deflection angles can reach 68.37°, 38.42°, and 28.29° when the phase gradients are 30°, 20°, and 15°, respectively.

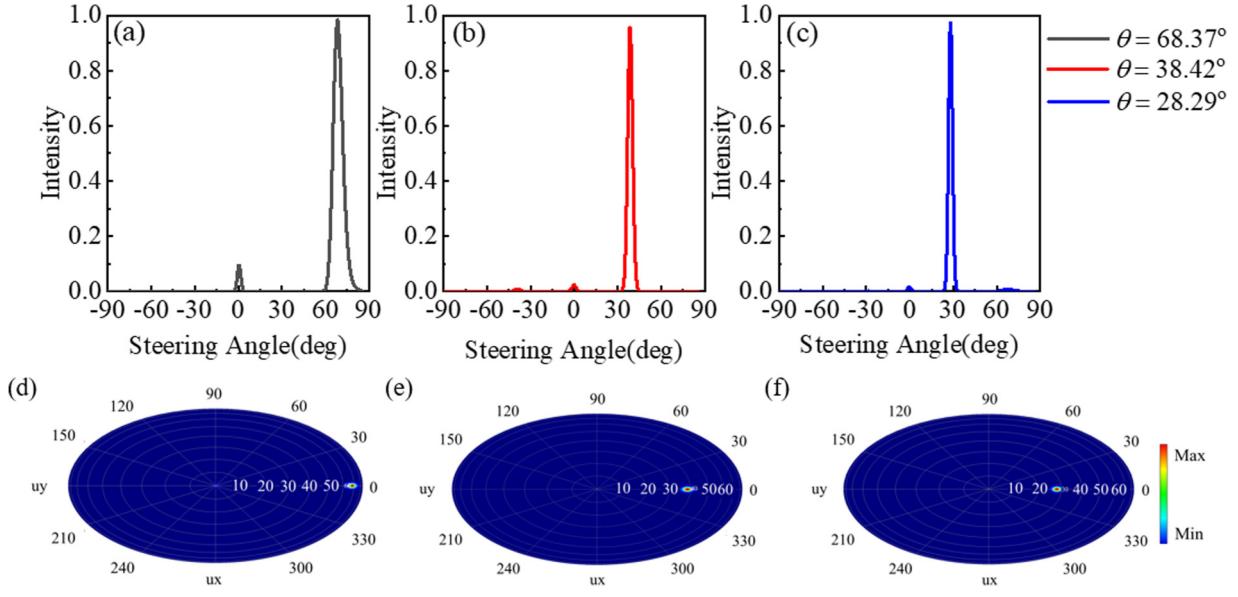

FIG. 8. Full-wave simulation results of the beam steering metasurface for (a) 68.37°, (b) 38.42°, and (c) 28.29° and far-field pattern of the beam steering metasurface for (d) 68.37°, (e) 38.42°, and (f) 28.29°.

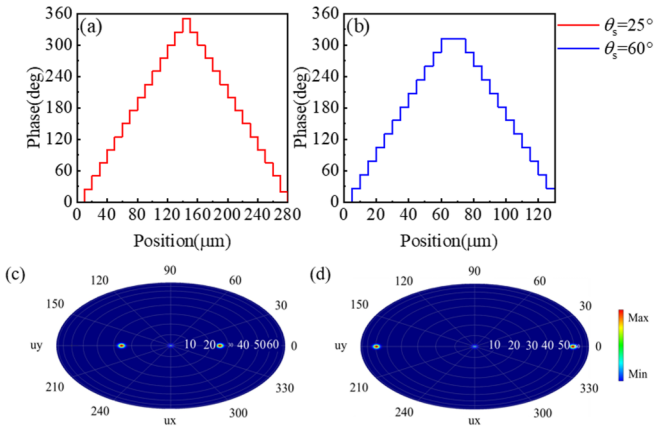

FIG. 9. Demonstration of a dynamic beam splitter: the spatial distribution of the phase shift at splitting angles of (a) 25° and (b) 60° and the far-field pattern of the TPA for beam splitting at angles of (c) 25.56° and (d) 59.29°

Because the design period of the metasurface element structure is only 5 μm, we can achieve sufficient phase regulation at 5.3 THz, so the value of the phase gradient is minimal, which is almost close to the value of the continuous phase curve. This also makes the simulated beam deflection angle consistent with the theoretical value. For other beam deflection angles, a similar method can be used to obtain different phase gradients by changing the graphene Fermi level of each supercell. After a large number of simulation experiments, it is concluded that the TPA can achieve fixed or continuous angle deflection in the range of 68.37° because the side-lobe energy will increase sharply when the deflection angle continues to increase. Further, within the maximum angle range, the maximum side-lobe energy is only 10% of the main lobe energy. This can make the device have a very high side mode rejection ratio, which is very favorable for future applications. In addition, it should be noted here that the TPA area in the simulation process is set to 600×600 μm^2 to ensure a sufficiently small spot waist radius and a clearer display of the quality and details of the spot because the total area of the TPA is only positively related to the spot waist radius.

C. TPA for beam splitting

The TPA based on the designed metasurface can also realize the function of adjustable beam splitting when VO_2 is in the metal phase. Using the same concept of controlling the phase imposed by each individual metasurface supercell, we are able to demonstrate the use of our multifunctional metasurface as a beam splitter by developing phase profiles for different beam splitting angles. Figures 9(a) and 9(b) show the spatial distribution of the phase shift to split the incident beam into a reflected beam at angles of 25° and 60°, respectively. These values are extracted from the relationship between the emergence angles and phase by the equations [48,49]

$$n_r \sin\theta_{r1} = n_i \sin\theta_i - \frac{c}{2\pi f}\frac{d\varphi_1}{dx},$$
$$n_r \sin\theta_{r2} = n_i \sin\theta_i - \frac{c}{2\pi f}\frac{d\varphi_2}{dx}, \quad (6)$$

where f is the incident electromagnetic wave frequency, c is the speed of light, θ_i is the incident angle, θ_{r1} and θ_{r2} are the angles of emergence of the left and right beams, respectively, n_i and n_r are the refractive indices of the incident and refractive media, respectively, and $d\varphi_1$ and $d\varphi_2$ are the phase changes along the left and right sides with respect to the center origin, respectively. To investigate the beam splitting performance, we simulate the multifunctional metasurface under the applied phase distributions illustrated in Figs. 9(a) and 9(b). Figures 9(c) and 9(d) illustrate the far-field pattern of the beam reflected from our TPA. The TPA can split the reflected light at angles of 25.56° and 59.29° when appropriate graphene Fermi levels are applied to the individual metasurface supercell.

IV. CONCLUSION

We have designed and demonstrated an electrically and thermally tunable hybrid multifunctional metasurface in the THz regime. The multifunctional metasurface is realized by incorporating the graphene pattern and VO_2 layer into the metasurface and is capable of spatiotemporal modulation of the fundamental attributes of the incident electromagnetic wave. As a proof of concept, we set up two modes for the multifunctional metasurface. When VO_2 is in the dielectric state and the graphene Fermi level is 0.35 eV, this metasurface represents the characteristics of the dual-band band-stop filter, which has 12.1% and 6.2% transmittance at 4.87 and 5.45 THz, respectively, while having high transmittance at other frequencies between 3.0 and 7.5 THz. By changing the Fermi energy level of graphene, these two band-stop frequencies will change in the range of 4.11–6.51 THz. When VO_2 is in the metal state, this metasurface turns into a TPA, which can realize the functions of beam deflection and beam splitting using the same device via controlling each supercell individually. The simulation results show that by changing the Fermi level of graphene, the metasurface array can achieve a specific deflection angle or continuous scanning in the range of 0–68.37° while the maximum side-lobe energy is only 10% of the main lobe energy. Moreover, when the phase distribution is changed, the metasurface array also demonstrates the beam splitting function with angles of 25.56° and 59.29°, respectively. Further, being all solid state, our device allows high-speed operation, robustness against mechanical impact, and scalability. With excellent magnetron sputtering deposition, CVD technology, wetting transfer technology, and gas plasma etching technology, our multifunctional metasurface array design method and architecture could facilitate the development of practical and commercially integrated on-chip electro-optical devices.

Data underlying the results presented in this paper are not publicly available at this time but may be obtained from the authors upon reasonable request.

ACKNOWLEDGMENTS

This research was supported by the National Key Scientific Instrument and Equipment Development Projects of

China (Grant No. 62027823), the Shenzhen Fundamental Research Program (Grant No. JCYJ2020109150808037), and the National Natural Science Foundation of China (Grant No. 61775048).

[1] J. Hebling, K.-L. Yeh, M. C. Hoffmann, and K. A. Nelson, High-power THz generation, THz nonlinear optics, and THz nonlinear spectroscopy, IEEE J. Sel. Top. Quantum Electron. **14**, 345 (2008).

[2] I. Pupeza, R. Wilk, and M. Koch, Highly accurate optical material parameter determination with THz time-domain spectroscopy, Opt. Express **15**, 4335 (2007).

[3] Y. Yang, H. Liu, M. Yang, B. Cui, and W. Zhang, Dielectric sphere-coupled THz super-resolution imaging, Appl. Phys. Lett. **113**, 031105 (2018).

[4] H. Yuan, D. Voß, A. Lisauskas, D. Mundy, and H. G. Roskos, 3D Fourier imaging based on 2D heterodyne detection at THz frequencies, APL Photon. **4**, 106108 (2019).

[5] R. Cheng, L. Xu, X. Yu, L. Zou, Y. Shen, and X. Deng, High-sensitivity biosensor for identification of protein based on terahertz Fano resonance metasurfaces, Opt. Commun. **473**, 125850 (2020).

[6] Y. Yang, D. Xu, and W. Zhang, High-sensitivity and label-free identification of a transgenic genome using a terahertz metabiosensor, Opt. Express **26**, 31589 (2018).

[7] S. Koenig, D. Lopez-Diaz, J. Antes, F. Boes, R. Henneberger, A. Leuther, A. Tessmann, R. Schmogrow, D. Hillerkuss, R. Palmer *et al.*, Wireless sub-THz communication system with high data rate, Nat. Photon. **7**, 977 (2013).

[8] Z. Wang, G. Dong, S. Yuan, L. Chen, X. Wu, and X. Zhang, Voltage-actuated thermally tunable on-chip terahertz filters based on a whispering gallery mode resonator, Opt. Lett. **44**, 4670 (2019).

[9] Z. Wei, X. Li, J. Yin, R. Huang, Y. Liu, W. Wang, H. Liu, H. Meng, and R. Liang, Active plasmonic band-stop filters based on graphene metamaterial at THz wavelengths, Opt. Express **24**, 14344 (2016).

[10] S. F. Zhou, L. Reekie, H. P. Chan, Y. T. Chow, P. S. Chung, and K. M. Luk, Characterization and modeling of Bragg gratings written in polymer fiber for use as filters in the THz region, Opt. Express **20**, 9564 (2012).

[11] X. Fu, F. Yang, C. Liu, X. Wu, and T. J. Cui, Terahertz beam steering technologies: From phased arrays to field-programmable metasurfaces, Adv. Opt. Mater. **8**, 1900628 (2020).

[12] D. Headland, Y. Monnai, D. Abbott, C. Fumeaux, and W. Withayachumnankul, Tutorial: Terahertz beamforming, from concepts to realizations, APL Photon. **3**, 051101 (2018).

[13] J. O'Hara and D. Grischkowsky, Synthetic phased-array terahertz imaging, Opt. Lett. **27**, 1070 (2002).

[14] M. Beruete and I. Jáuregui-López, Terahertz sensing based on metasurfaces, Adv. Opt. Mater. **8**, 1900721 (2020).

[15] X. Liu, K. Fan, I. V. Shadrivov, and W. J. Padilla, Experimental realization of a terahertz all-dielectric metasurface absorber, Opt. Express **25**, 191 (2017).

[16] S.-F. Shi, B. Zeng, H.-L. Han, X. Hong, H.-Z. Tsai, H. Jung, A. Zettl, M. Crommie, and F. Wang, Optimizing broadband terahertz modulation with hybrid graphene/metasurface structures, Nano Lett. **15**, 372 (2015).

[17] X. Zhao, J. Schalch, J. Zhang, H. R. Seren, G. Duan, R. D. Averitt, and X. Zhang, Electromechanically tunable metasurface transmission waveplate at terahertz frequencies, Optica **5**, 303 (2018).

[18] D. Hu, X. Wang, S. Feng, J. Ye, W. Sun, Q. Kan, P. J. Klar, and Y. Zhang, Ultrathin terahertz planar elements, Adv. Opt. Mater. **1**, 186 (2013).

[19] X.-Y. Jiang, J.-S. Ye, J.-W. He, X.-K. Wang, D. Hu, S.-F. Feng, Q. Kan, and Y. Zhang, An ultrathin terahertz lens with axial long focal depth based on metasurfaces, Opt. Express **21**, 30030 (2013).

[20] Z. Shen, S. Zhou, S. Ge, W. Duan, P. Chen, L. Wang, W. Hu, and Y. Lu, Liquid-crystal-integrated metadevice: Towards active multifunctional terahertz wave manipulations, Opt. Lett. **43**, 4695 (2018).

[21] S.-T. Xu, F. Fan, Y.-Y. Ji, J.-R. Cheng, and S.-J. Chang, Terahertz resonance switch induced by the polarization conversion of liquid crystal in compound metasurface, Opt. Lett. **44**, 2450 (2019).

[22] L. Cong, Y. K. Srivastava, H. Zhang, X. Zhang, J. Han, and R. Singh, All-optical active THz metasurfaces for ultrafast polarization switching and dynamic beam splitting, Light Sci. Appl. **7**, 28 (2018).

[23] Z. Song and J. Zhang, Achieving broadband absorption and polarization conversion with a vanadium dioxide metasurface in the same terahertz frequencies, Opt. Express **28**, 12487 (2020).

[24] Q. Wang, E. T. Rogers, B. Gholipour, C.-M. Wang, G. Yuan, J. Teng, and N. I. Zheludev, Optically reconfigurable metasurfaces and photonic devices based on phase change materials, Nat. Photon. **10**, 60 (2016).

[25] M. Amin, O. Siddiqui, H. Abutarboush, M. Farhat, and R. Ramzan, A THz graphene metasurface for polarization selective virus sensing, Carbon **176**, 580 (2021).

[26] X. Chen, Z. Tian, Y. Lu, Y. Xu, X. Zhang, C. Ouyang, J. Gu, J. Han, and W. Zhang, Electrically tunable perfect terahertz absorber based on a graphene Salisbury screen hybrid metasurface, Adv. Opt. Mater. **8**, 1900660 (2020).

[27] J. Zhao, J. Song, T. Xu, T. Yang, and J. Zhou, Controllable linear asymmetric transmission and perfect polarization conversion in a terahertz hybrid metal-graphene metasurface, Opt. Express **27**, 9773 (2019).

[28] Y. Fan, N.-H. Shen, T. Koschny, and C. M. Soukoulis, Tunable terahertz meta-surface with graphene cut-wires, ACS Photon. **2**, 151 (2015).

[29] K. Yang, S. Liu, S. Arezoomandan, A. Nahata, and B. Sensale-Rodriguez, Graphene-based tunable metamaterial terahertz filters, Appl. Phys. Lett. **105**, 093105 (2014).

[30] B. Orazbayev, M. Beruete, and I. Khromova, Tunable beam steering enabled by graphene metamaterials, Opt. Express **24**, 8848 (2016).

[31] F. Ding, S. Zhong, and S. I. Bozhevolnyi, Vanadium dioxide integrated metasurfaces with switchable functionalities at terahertz frequencies, Adv. Opt. Mater. **6**, 1701204 (2018).

[32] J. Huang, J. Li, Y. Yang, J. Li, J. Li, Y. Zhang, and J. Yao, Active controllable bandwidth of THz metamaterial bandpass filter based on vanadium dioxide, Opt. Commun. **465**, 125616 (2020).

[33] G. Kaplan, K. Aydin, and J. Scheuer, Dynamically controlled plasmonic nano-antenna phased array utilizing vanadium dioxide, Opt. Mater. Express **5**, 2513 (2015).

[34] L. Ju, B. Geng, J. Horng, C. Girit, M. Martin, Z. Hao, H. A. Bechtel, X. Liang, A. Zettl, Y. R. Shen *et al.*, Graphene plasmonics for tunable terahertz metamaterials, Nat. Nanotechnol. **6**, 630 (2011).

[35] R. Kargar, K. Rouhi, and A. Abdolali, Reprogrammable multifocal THz metalens based on metal–insulator transition of VO2-assisted digital metasurface, Opt. Commun. **462**, 125331 (2020).

[36] J. Li, Y. Zhang, J. Li, J. Li, Y. Yang, J. Huang, C. Ma, Z. Ma, Z. Zhang, L. Liang, and J. Yao, Frequency-switchable VO_2-based coding metasurfaces at the terahertz band, Opt. Commun. **458**, 124744 (2020).

[37] B. Sensale-Rodriguez, R. Yan, L. Liu, D. Jena, and H. G. Xing, Graphene for reconfigurable terahertz optoelectronics, Proc. IEEE **101**, 1705 (2013).

[38] Y. Zhang, Y. Feng, and J. Zhao, Graphene-enabled tunable multifunctional metamaterial for dynamical polarization manipulation of broadband terahertz wave, Carbon **163**, 244 (2020).

[39] R. Zhou, T. Jiang, Z. Peng, Z. Li, M. Zhang, S. Wang, L. Li, H. Liang, S. Ruan, and H. Su, Tunable broadband terahertz absorber based on graphene metamaterials and VO_2, Opt. Mater. **114**, 110915 (2021).

[40] M. Huang, Y. Cheng, Z. Cheng, H. Chen, X. Mao, and R. Gong, Based on graphene tunable dual-band terahertz metamaterial absorber with wide-angle, Opt. Commun. **415**, 194 (2018).

[41] T.-T. Kim, H.-D. Kim, R. Zhao, S. S. Oh, T. Ha, D. S. Chung, Y. H. Lee, B. Min, and S. Zhang, Electrically tunable slow light using graphene metamaterials, ACS Photon. **5**, 1800 (2018).

[42] B. Sensale-Rodriguez, R. Yan, S. Rafique, M. Zhu, W. Li, X. Liang, D. Gundlach, V. Protasenko, M. M. Kelly, D. Jena *et al.*, Extraordinary control of terahertz beam reflectance in graphene electro-absorption modulators, Nano Lett. **12**, 4518 (2012).

[43] S. H. Lee, M. Choi, T.-T. Kim, S. Lee, M. Liu, X. Yin, H. K. Choi, S. S. Lee, C.-G. Choi, S.-Y. Choi *et al.*, Switching terahertz waves with gate-controlled active graphene metamaterials, Nat. Mater. **11**, 936 (2012).

[44] Z. Song, Y. Deng, Y. Zhou, and Z. Liu, Terahertz toroidal metamaterial with tunable properties, Opt. Express **27**, 5792 (2019).

[45] Q. Qian, L. Fan, L. Zhao, and C. Wang, Non-metallic and angular-insensitive metasurface transmissive long-pass filter in the visible and near-infrared regions, Opt. Lett. **45**, 359 (2020).

[46] B. M. Wells, F. Lotti, M. E. Nasir, A. V. Zayats, and V. A. Podolskiy, Angle-insensitive plasmonic nanorod metamaterial-based band-pass optical filters, Opt. Express **29**, 11562 (2021).

[47] J. Park, B. G. Jeong, S. I. Kim, D. Lee, J. Kim, C. Shin, C. B. Lee, T. Otsuka, J. Kyoung, S. Kim *et al.*, All-solid-state spatial light modulator with independent phase and amplitude control for three-dimensional LiDAR applications, Nat. Nanotechnol. **16**, 69 (2021).

[48] M. Wei, Q. Xu, Q. Wang, X. Zhang, Y. Li, J. Gu, Z. Tian, X. Zhang, J. Han, and W. Zhang, Broadband non-polarizing terahertz beam splitters with variable split ratio, Appl. Phys. Lett. **111**, 071101 (2017).

[49] X. Zhang, R. Deng, F. Yang, C. Jiang, S. Xu, and M. Li, Metasurface-based ultrathin beam splitter with variable split angle and power distribution, ACS Photon. **5**, 2997 (2018).